



FINAL REPORT

Preserving Coastal Infrastructure through the Design and Implementation of Image-Based Structural Health Monitoring (iSHM)

Date: January 2019

Prepared by:

Devin K. Harris, Ph.D., Associate Professor
Mehrdad Shafiei Dizaji, Graduate Research Assistant
Department of Civil and Environmental Engineering
University of Virginia
351 McCormick Rd Thornton Hall
Charlottesville, VA 22904

Prepared for:

Mid-Atlantic Transportation Sustainability Center – Region 3 University Transportation Center
US Department of Transportation
Office of the Secretary-Research
UTC Program, RDT-30
1200 New Jersey Ave., SE
Washington, DC 20590

1. Report No.	2. Government Accession No.	3. Recipient's Catalog No.	
4. Title and Subtitle Preserving Coastal Infrastructure through the Design and Implementation of Image-Based Structural Health Monitoring (iSHM)		5. Report Date 2/13/2019	
		6. Performing Organization Code	
7. Author(s) Devin K. Harris, Ph.D. Mehrdad Shafiei Dizaji		8. Performing Organization Report No.	
9. Performing Organization Name and Address Department of Civil and Environmental Engineering University of Virginia 351 McCormick Rd Thornton Hall Charlottesville, VA 22904		10. Work Unit No. (TRAIS)	
		11. Contract or Grant No.	
12. Sponsoring Agency Name and Address US Department of Transportation Office of the Secretary-Research UTC Program, RDT-30 1200 New Jersey Ave., SE Washington, DC 20590		13. Type of Report and Period Covered Final 8/1/16 – 8/31/18	
		14. Sponsoring Agency Code	
15. Supplementary Notes			
16. Abstract This report describes the outcomes on an investigation aimed at leveraging image-based measurement, namely three-dimensional digital image correlation (3D-DIC), with a structural health monitoring framework. This work aligns with a thrust in the emerging area of image-based structural health monitoring (iSHM) and offers the potential for a low-cost high impact assessment technique for characterizing the operational response of existing structures (i.e. bridge, culverts, and ancillary structures) with minimal service disruption and without the need for extensive instrumentation and monitoring equipment. This investigation highlights the results of an experimental laboratory study that integrates the full-field three-dimensional surface deformation response of selected steel members within a structural identification (St-ID) framework. Results from 3D-DIC measurements are mapped to a common spatial grid in parallel with the results from a 3D finite element model, and an optimization routine is employed to minimize and objective function, which in turn updates uncertain parameters within the model. The updated parameters serve as the results for the St-ID framework proposed and highlight the benefits derived form a full-field updating approach over conventional discrete sensors.			
17. Key Words digital image correlation, structural identification, structural health monitoring, optimization, St-ID, SHM		18. Distribution Statement No restrictions. This document is available from the National Technical Information Service, Springfield, VA 22161	
19. Security Classif. (of this report) Unclassified	20. Security Classif. (of this page) Unclassified	21. No. of Pages 28	22. Price

DISCLAIMER

The contents of this report reflect the views of the authors, who are responsible for the facts and the accuracy of the information presented herein. This document is disseminated under the sponsorship of the U.S. Department of Transportation's University Transportation Centers Program, in the interest of information exchange. The U.S. Government assumes no liability for the contents or use thereof.

TABLE OF CONTENTS

Disclaimer	3
Table of Contents	4
List of Figures	5
List of Tables	6
Introduction	7
Background and Literature Review	8
Basis of Structural Health Monitoring	8
Structural Identification within SHM Framework	8
Vision-Based Sensing	9
Digital Image Correlation	9
Project Scope	10
Research Approach	11
Experimental Investigation	11
Experimental Setup	13
3D-DIC Setup	14
Loading regime	16
Numerical Simulation	16
Results	17
DIC results versus reference sensors	17
Structural identification using FEMU with DIC via hybrid optimization algorithm	19
Definition of the objective function	19
Optimization Process- Hybrid Genetic Algorithm (HGA)	20
Solution Convergence	21
Performance of Updated FE Model	24
Conclusion	25
Recommendations and Future Work	26
References	26

LIST OF FIGURES

Figure 1 – Hampton Roads Bridge Tunnel (a) approach span and (b) deterioration.....	7
Figure 2 – Schematic of Digital Image Correlation.....	10
Figure 3 – Overview of Proposed Vision-Based St-ID	11
Figure 4 - Schematic of the steel beam (a) loading and boundary conditions used during experimental testing (b) Configuration 1 (c) Configuration 2 (d) Configuration 3	12
Figure 5 - Boundary and loading fixtures (a) different supports used in the tested configurations (b) supports used for the first configuration (c) supports used for the second configuration (d) support used for the third configuration.....	13
Figure 6 - Experimental setup (a) MTS software, actuator, beam setup and DIC software; (b) 6 camera setup (3 systems or 3 camera pairs) 1 pair at midspan (8 mm lens) and 1 pair at each support (12 mm lens) (c) DIC and instrumentation configuration	14
Figure 7 - Diagram of the optical setup	15
Figure 8 - Camera configuration (a) DIC camera setup (b) Field of view, speckle pattern and subsets.....	16
Figure 9 - Isometric view of representative finite element model of the steel beam (Configuration 1 shown).....	17
Figure 10 - Longitudinal (ϵ_{xx}) DIC strain fields at the maximum load, $t=150$ sec, frame#300....	18
Figure 11 - Comparison of results obtained from DIC and mechanical sensors (a) midspan strain; (b) midspan deflection; (c) right support deflection; (d) left support deflection	18
Figure 12 - Overview of the proposed Hybrid-Genetic Algorithm	20
Figure 13 - Evolution of unknown parameter convergence versus iterations for CF1B (a) Cost Function (b) Modulus of Elasticity (c) $K1, K2$ (d) $K3, K4$	22
Figure 14 - Contour plots of the experimental strain fields, the numerical strain fields and their absolute difference for the middle span for the components $\epsilon_{xx}, \epsilon_{xy}, \delta y$ at $t=150$ sec for CF1B.....	23
Figure 15 - Contour plots of the experimental strain fields, the numerical strain fields and their absolute difference for the component δy (first row for left support and second row for right support) at $t=150$ sec for CF1B.....	24
Figure 16 - Comparison of the evolution of the longitudinal strains ϵ_{xx} for CFB1 between the numerically computed values and the values obtained using DIC at points A-B shown in fig. 8, for (a) before model updating, (b) after updating	25

LIST OF TABLES

Table 1 - Initial, minimum and maximum values of the updating parameters	21
Table 2 - Parameters of the genetic algorithm (GA) for the three identification tests for the first configuration	21
Table 3 - Identified optimal parameters based on Hybrid Genetic Algorithm for different parameters of the GA for the first configuration	21
Table 4 - Identified optimal parameters for different configurations for group B set of parameters of the GA.....	23

INTRODUCTION

With infrastructure systems across the globe approaching the end of their service lives, there is an ever-pressing need for techniques to assess current condition and remaining life. As a case in point, bridges in the United States, with an average age approaching 45 years, represent one particular infrastructure system that is at risk [1]. In the Commonwealth of Virginia, the Virginia Department of Transportation (VDOT) is responsible for the design, maintenance, and repair/replacement of the bridge infrastructure components that make up part of the transportation network. Like many other states, VDOT has taken an aggressive approach to managing its bridge inventory by establishing a global performance measure based on structural deficiency, which aims to ensure that no more than 8% of their inventory is rated as structurally deficient. This global performance metric has outpaced the national average, with consistent reductions in structural deficiency from year to year. However, despite these types of initiatives, deterioration often outpaces solutions for preservation and owners are faced with the challenges of assessing and managing this infrastructure without the resources and staffing necessary for proper management. This feature is particularly critical in regions such as Hampton Roads (Figure 1), where high profile infrastructure systems such as the Hampton Road Bridge Tunnel and Chesapeake Bay Bridge provide critical linkages along the Mid-Atlantic coastal corridor. The infrastructure in these critical regions are particularly vulnerable to environmental change such as sea level rise extreme weather events, which not only has the potential to impact daily and event driven operation, but also impact the long-term performance as these structures are exposed to more extreme operational demands. Examples of these extreme operational demands include: greater thermal cycles, more exposure to salting during snowstorm events, topside seawater exposure from storm surges, and underside exposure saltwater spray.



Figure 1 – Hampton Roads Bridge Tunnel (a) approach span and (b) deterioration

Assessment represents one of the key components of the broader framework of structural health monitoring and is essential to an overall mission of transportation sustainability, specifically infrastructure sustainability. Within the context of infrastructure preservation, assessment provides owners and infrastructure managers with a basis to make performance-based decisions and allocate resources. Integrated within the context of assessment is the ability to measure condition state and translate these observations into descriptions of behavior.

BACKGROUND AND LITERATURE REVIEW

Basis of Structural Health Monitoring

Structural health monitoring (SHM) provides a general framework for characterizing the performance of existing structures within their operational condition state. While the foundation of this foundation is sound, SHM has not gained sufficient traction in the transportation community for a number of reasons. Many of the reason attributed to the limited adoption of SHM include the slow rates of change of transportation structures, cost of SHM systems, expertise required to interpret data derived, longevity of monitoring systems, and challenges associated with resolving damage within large scale systems. SHM has existed for several years in various forms across multiple engineering disciplines [2] and has been likened to a human health management system [3], with well-person checkups, preventative intervention, and treatment/surgery being analogized to inspection, maintenance, and repair/retrofit, respectively. Over the years, a large body of research has been performed on condition assessment [4, 5] and SHM [6] of infrastructure with advances in novel technologies [7-9] and assessment techniques [10-12]. These advances illustrated that the body of knowledge in SHM has grown considerably over the past few decades, but a fundamental challenge that remains is the translation of measurable phenomena derived from full-scale physical systems into information that describes the system's health and condition state.

Structural Identification within SHM Framework

Within this aforementioned SHM framework, numerical models, typically finite element models (FEM), are commonly used in collaboration with sensing to describe the behavior of structural systems. FEM has been used with great success to simulate structural response of idealized systems, but its approximate nature and simplifying assumptions coupled with uncertainties associated with boundary conditions and condition state inherently result in errors when describing existing structural systems [13]. Structural identification (St-ID) describes an approach that emphasizes correlation of the response characteristics between a model and experiment or measurement, providing a basis for using an updated FE model to characterize critical performance measures of existing structural systems. St-ID is the solution to an inverse problem and aims to minimize differences between analytical and experimental results. This solution is typically formulated as an optimization problem, with an objective of identifying the unknown or uncertain features within the problem space. Satisfactory correlation between the observed experimental behavior and the analytical results is critical, but equally essential is maintaining the physical significance of updated parameters [14]. For this purpose, setting up of an objective or cost function and selecting updating parameters are crucial steps in St-ID. The changes in these parameters are then determined iteratively and pushed to a minimum via an optimization algorithm. St-Id aims to bridge the gap between the model and the real system by developing reliable estimates of the performance and vulnerability through improved simulations.

In many St-ID scenarios a cost function is developed and defined in terms of differences between numerical and experimental displacement fields. This function is then minimized on part of the system boundary in an iterative manner, for example by changing the material parameters and boundary conditions. Given a unique set of system geometry, material parameters, traction and displacement boundary conditions, the displacement and deformation response of a system is also unique. Hence, assuming the system geometry and boundary conditions are correctly replicated in the Finite Element (FE) model, convergence between numerical and experimental displacement fields is achieved only when the constitutive parameters approach their true values.

Examples of this optimization concept are available across numerous fields, but representative St-ID examples are available in the literature [15-17]. Within the context of in-service infrastructure systems, St-ID provides a pathway by which the operational response characteristics of a system can be used to characterize performance of the system within its environment.

Vision-Based Sensing

A basic step in a SHM framework involves measuring the behavior of the structure, usually in the form of deflections, strains or accelerations. This work focuses primarily on the measurement of deformations using a specific vision-based sensing modality, digital image correlation (DIC). While other techniques could provide representative measurements, DIC provides a unique output, namely full-field measurement, which aligns directly with the full-field results derived from FEA. This presents a unique capability for full-field St-ID that cannot be realized with other measurement approaches.

Digital Image Correlation

The ability to measure deformation is vital to the field of engineering mechanics; however, historical practice has often been limited to localized deformation measurement tools such as strain gauges, linear variable displacement transducers and vibrating wire gauges [18-20]. While these measurement techniques have been used extensively in SHM and St-ID in the past, recent advances in photogrammetric and image-based measurement techniques [21-23] provide an alternative strategy for describing structural response and characterizing deformations [24]. These image-based techniques have shown great promise for describing the behavior [25-31] and condition state [5, 32, 33] of civil infrastructure systems due to their non-contact nature, relative ease of deployment, and recent improvement of imaging technologies.

DIC extends the principles of photogrammetry and can be described as a full-field non-contact surface measurement technique that utilizes image correlation and tracking techniques on a series of sequential images to describe in-plane deformation, and movement of a specimen subjected to loading [34]. Surface displacement data, which can be transformed into strain via post-processing, is derived by comparing sequential pairs of digital images taken before and after the deformation. Images can be derived from a variety of sources (e.g. CCD, DSLR, etc.) with the choice of camera and lens configuration influenced by factors such as camera noise, lighting, acquisition speed, and geometric relationships between area of interest and field of view. Figure 2, provides a basic schematic of the DIC concept. This approach can be performed in two dimensions using a single camera to provide in-plane deformation or in three dimensions using stereo-paired cameras to provide in-plane and out-of-plane deformations. Additionally, recent advances in imaging has enable the measurement of 3D dynamic response using the same technique. A comprehensive treatment of DIC is available in the literature and not presented here.

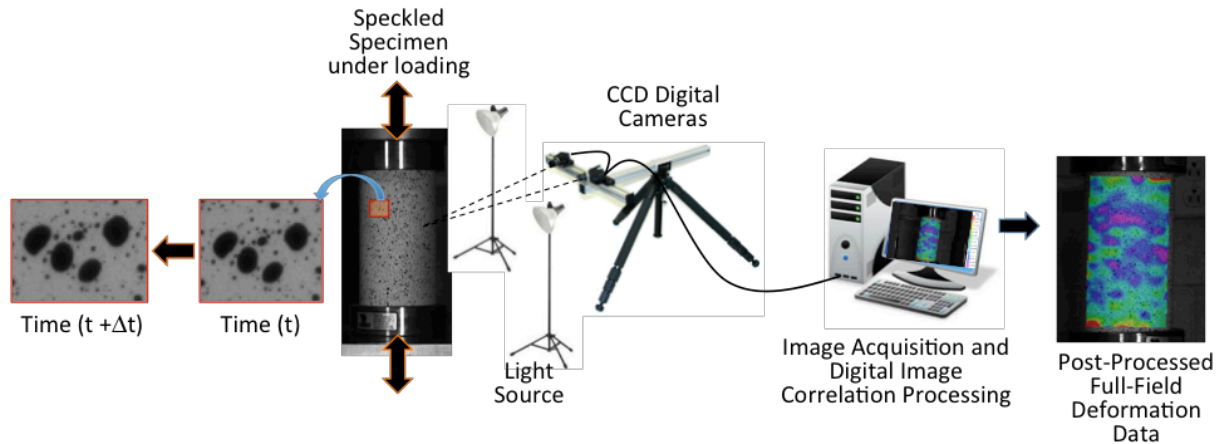


Figure 2 – Schematic of Digital Image Correlation

PROJECT SCOPE

Historically, much of the assessment strategies used to define performance have relied heavily on visual inspection as the standard method to characterize condition state, but research has shown that visual inspections yield results that are subjective and somewhat unreliable. Additionally, these condition characterization approaches only provide a description of damage, but do not link to performance. On the other front of evaluation, there has been a major push in the area of sensing techniques and sensors, but these advances have also not succeeded in bridging the gap between measurement and performance. In recent years, there have been significant advances in the field of vision-based sensing [35]. While traditional visual assessment has a number of limitations when used in a subjective manner, vision as a quantitative tool has a number benefits for assessment including:

- vision-based assessment is a non-contact technique that requires limited access;
- vision-based assessment is also non-invasive, not requiring physical instrumentation;
- advances in vision-based measurement is able to describe;
- quantitative vision-based techniques align with historical practices of qualitative vision-based inspection;
- condition and behavior features can be linked over time scales

This investigation explored a novel concept that leverage advances in vision-based assessment to develop and approach for integration into the domain of structural health monitoring. This work aligns with a thrust in the emerging area of image-based structural health monitoring (iSHM) and offers the potential for a low-cost high impact assessment technique for characterizing the operational response of existing structures (i.e. bridge, culverts, and ancillary structures) with minimal service disruption and without the need for extensive instrumentation and monitoring equipment. Within the scope of this work, the capabilities of vision-based deformation measurement approaches for describing condition state, system behavior, damage identification, and model updating were evaluated. A basic schematic of the vision-based St-ID framework is illustrated in Figure 3.

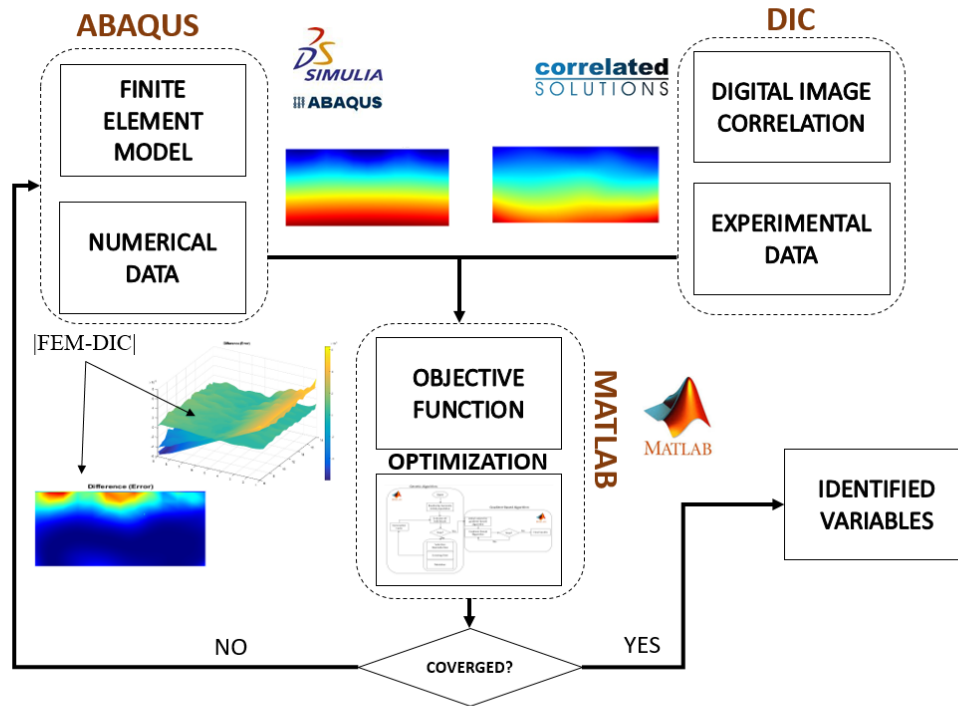


Figure 3 – Overview of Proposed Vision-Based St-ID

RESEARCH APPROACH

The research approach leveraged a small scale experimental program to evaluate the feasibility of leveraging 3D-DIC in a St-ID/SHM framework. This work has been presented in other publication formats and more detail is available in these publications [36-39]; however, only a subset of these findings are presented in this report.

EXPERIMENTAL INVESTIGATION

The experimental program included to a laboratory scale investigation of a representative steel beam subjected to various loading and boundary conditions, and these experiments were aimed at evaluating the feasibility of vision-based St-ID at the structural member scale. The configurations used in this investigation are illustrated schematically in Figure 4 and can be described as:

- Configuration 1 (CF1): structural component simply supported subjected to concentrated load at midspan (Figure 4b).
- Configuration 2 (CF2): structural component simply supported under four-point loading with paired concentrated loads around midspan (Figure 4c).
- Configuration 3 (CF3): structural component with simple and partial support restraints subjected to a concentrated load at midspan (Figure 4d).

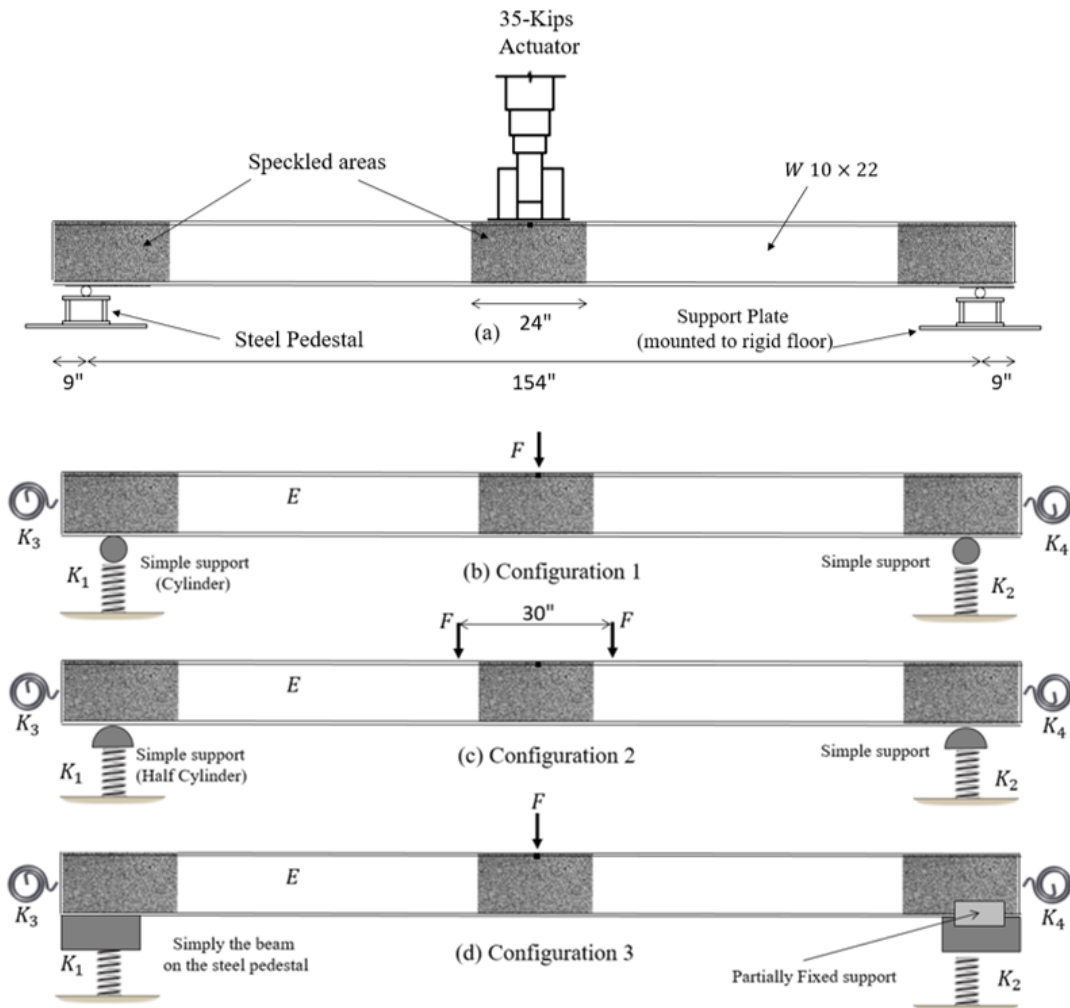


Figure 4 - Schematic of the steel beam (a) loading and boundary conditions used during experimental testing (b) Configuration 1 (c) Configuration 2 (d) Configuration 3

The restraint configurations illustrated in Figure 4 were intended to mimic idealized boundary and loading conditions and provide a basis for characterizing the differences these idealized conditions and real systems. Figure 5 shows the actual boundary and loading fixtures used in experimental set up for different configurations.

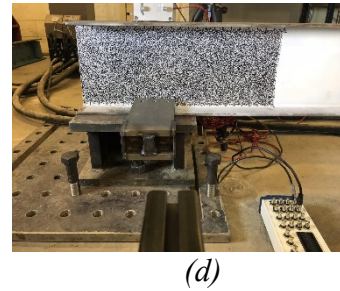
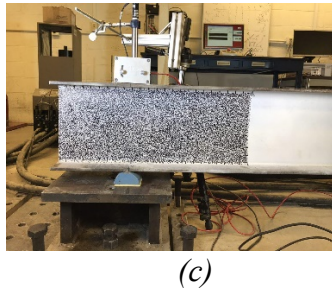
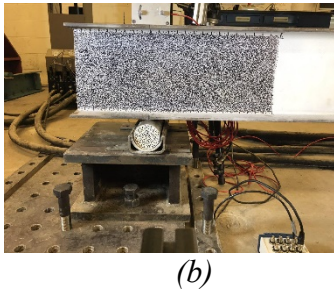
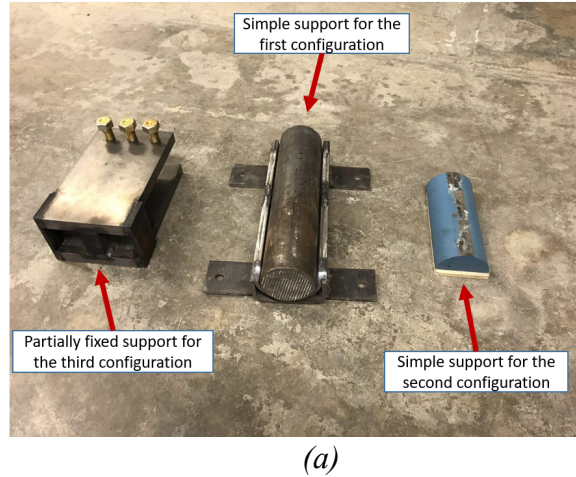


Figure 5 - Boundary and loading fixtures (a) different supports used in the tested configurations (b) supports used for the first configuration (c) supports used for the second configuration (d) support used for the third configuration

Experimental Setup

The experimental program consisted of a series of loading cycles within the elastic range ($\sigma_{yield} = 50$ ksi) of a wide-flange hot-rolled structural steel beam (ASTM A992 W10x22). The 172 in. long beam was tested in the Structures Laboratory at the University of Virginia and configured for strong-axis bending. The beam was instrumented with Bridge Diagnostic Inc. (BDI) sensors at both midspan and support locations to provide a comparison between traditional SHM sensing modalities and those derived from the 3D-DIC measurements (Correlated Solutions *VIC-3D*) at the same locations. Figure 6 provides a basic illustration of the experimental setup and instrumentation along with the DIC setup used during testing. Details on the DIC setup are described in more detail in the following sections.

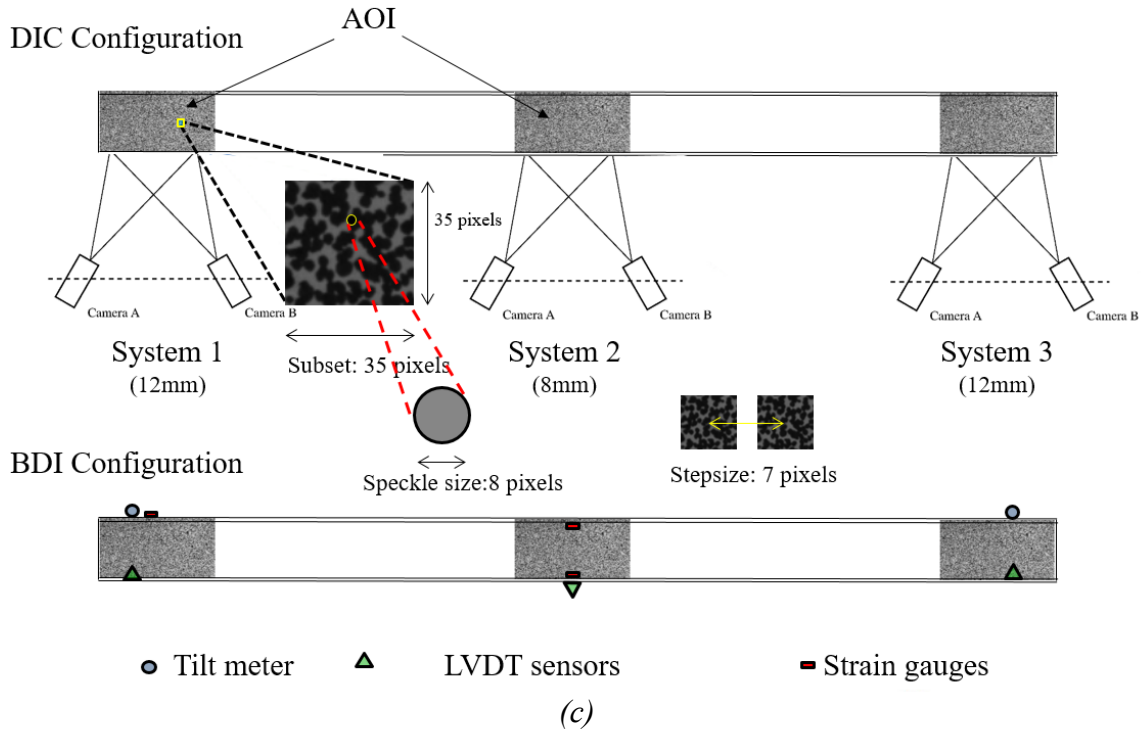


Figure 6 - Experimental setup (a) MTS software, actuator, beam setup and DIC software; (b) 6 camera setup (3 systems or 3 camera pairs) 1 pair at midspan (8 mm lens) and 1 pair at each support (12 mm lens) (c) DIC and instrumentation configuration

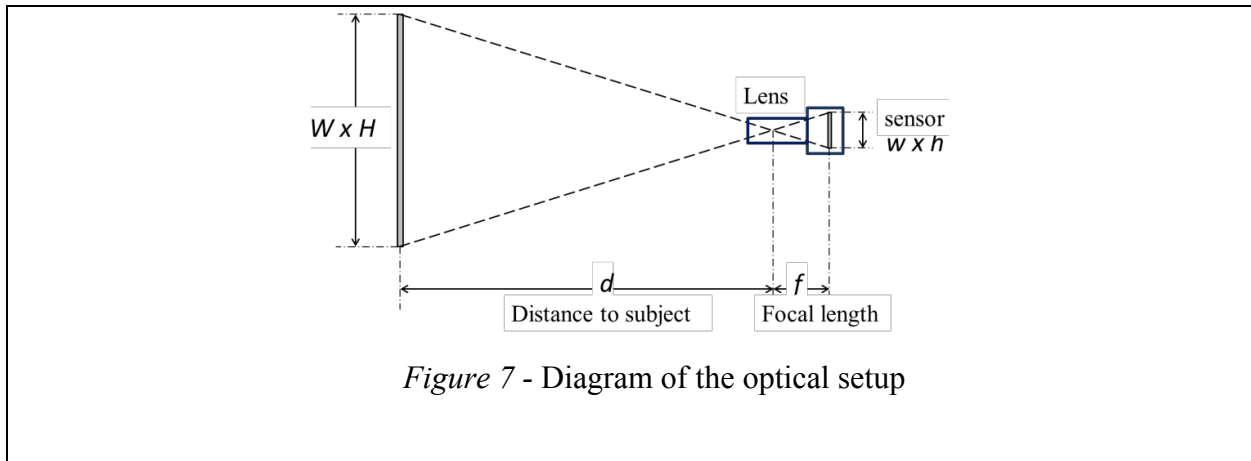
3D-DIC Setup

Three sets of two stereo-paired digital cameras (Point Grey Grasshopper 2.0) were used to evaluate the midspan (Schneider 8 mm lens) and two end span (Schneider 12 mm lenses) locations. The camera systems utilized different lens configurations due to the physical constraints of the load frame location relative to the test specimen. Each camera had a 5-megapixel charge coupled device (CCD) image sensor with a resolution of 2448×2048 . The image sensor for this camera was $2/3''$ format with dimensions of $0.35'' \times 0.26''$, which accounted for a pixel size of 1.36×10^{-4} inch. The camera was connected to a C-mount optical lens and the acquired data was communicated to the control PC through FireWire cables. To accommodate the specimen within the field of view of cameras with the highest resolution, the design on the imaging setup was achieved by considering the geometrical restraints of the laboratory space (maximum available space from cameras to the beam was about 50 inches) as well as the available optical lenses. Using 12 mm lenses for the end locations and 8 mm lenses for the middle location, the distance of the camera from the beam was calculated using Equation 1, where w/h is the sensor width/height, W/H is the field of view width/height, d is the distance to the object, and f is the focal length (Figure 7). Using the dimensions of the speckled region ($24'' \times 9.5''$) and leaving a space of at least one inch around each side of the region to accommodate deformations to be captured, the 8mm and 12mm lenses had to be placed at about $23.5''$ and $35''$ from the specimen (Figure 6), respectively, to produce comparable fields of view. The end and midspan locations were patterned over the full depth of the beam web over a 24 in. width, with the pattern created by applying a flat white paint base coat,

followed by random speckle pattern with a permanent marker (Figure 8b). To achieve a high spatial resolution of during the analysis while at the same time being large enough to be resolved in the images, the pattern had an average speckle size of 0.08 inch, which corresponds to approximately 8 pixels in the captured images. For the pixel tracking process in DIC, the area of interest on the speckle pattern was split into rectangular windows or “subsets” and unique patterns of speckles were available within each subset to allow for tracking in subsequent frames. The patterns in the subsets were tracked on a grid of a specific “step” size, which dictated the spatial resolution of the calculated points. To achieve a fine grid of unique patterns in subsets, the selection of the subset size was achieved through direct experimentation and a square subset of 35 pixels at a step of 7 pixels was selected.

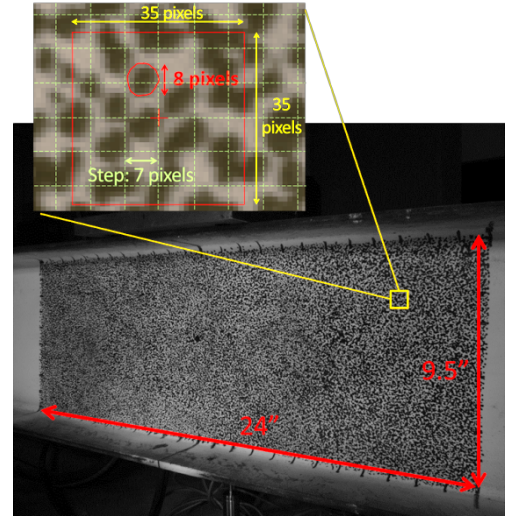
The DIC data acquisition (DAQ) integrated output signals (load and displacement) from MTS actuators and controller to allow for simultaneous acquisition of load, displacement, and images. The BDI DAQ system was not directly linked, but was synchronized manually at the start of each test. Figure 8 shows the basic geometric configuration of the 3D-DIC setups used in the experiments in addition to the basic post-processing characteristics of the DIC analysis.

$$\frac{w}{W} = \frac{h}{H} = \frac{f}{d} \quad \text{Equation 1}$$





(a)



(b)

Figure 8 - Camera configuration (a) DIC camera setup (b) Field of view, speckle pattern and subsets

Loading regime

For each of the configurations, the beam was loaded monotonically under displacement-control, with the beam response kept within the elastic range. The loading sequence consisted of loading the beam to a displacement of 0.05 inch at a rate of 0.002 inch per second, followed by a two-cycle sinusoidal loading from 0.05 inch up to a peak displacement of 0.3 inch, and concluding with an unloading through the reverse of the initial loading sequence. The initial loading and final unloading occurred over a period of 50 seconds (25 seconds each), while the sinusoidal sequence occurred over a period of 500 seconds (250 seconds for each cycle). The BDI DAQ collected data during the loading sequence at 100 Hz while the DIC images were acquired at 2 Hz which resulted in 1,143 images.

NUMERICAL SIMULATION

As previously noted, St-ID requires the development of an initial numerical model that can be updated based on experimentally derived behavior results. In this investigation, finite element models of each loading/boundary condition scenario were developed in ABAQUS, a robust commercially available finite element software package. For each scenario, the steel beam was modeled using a total of 4,300 Continuum 3D hexahedral solid elements (C3D8) with full integration. The geometry was developed from standard section properties available within the AISC Manual of Steel Construction. The boundary supports were modeled as a series of springs (translational and rotational) to represent the deviation from ideal simple and fixed conditions and to allow for updating based on experimental measurements. A global view of the model of the steel beam is shown in Figure 9. With the model representing a relatively non-complex structural component, a dense mesh was not required; however, the mesh density was initially developed and later refined to allow for alignment with the coordinate system of the DIC results. It should be noted that ABAQUS allowed for the development of a direct interface with MATLAB, a multi-paradigm numerical computing environment, which facilitated the iterative parameter optimization algorithm.

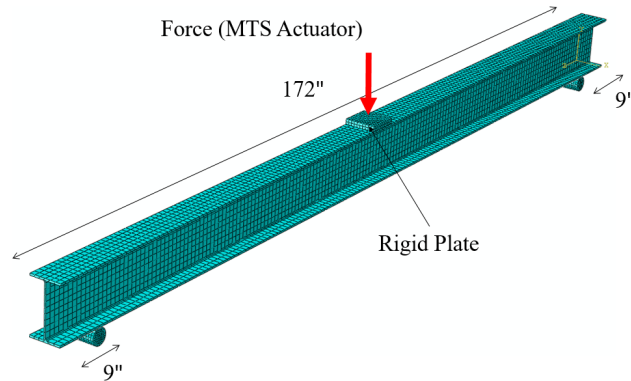


Figure 9 - Isometric view of representative finite element model of the steel beam (Configuration 1 shown)

RESULTS

DIC results versus reference sensors

Results from the experimental program provided a basis for comparison of the 3D-DIC measurements with the mechanical sensors that are representative of those used in traditional structural testing and SHM applications. For the comparison, a virtual gauge was selected in the DIC system to allow for local strains to be measured within both the tension and compression regions of the cross-section as shown in Figure 8. The evolution of strains (ϵ_{xx}) at the two locations, A and B (Figure 10), along with the corresponding vertical deflection were extracted from DIC results. Similarly, results from the support locations were extracted from the DIC; however, for this location, only displacements were considered as the strains near the supports are relatively low. Figure 11 illustrates a comparison of the results of selected sensors for one of the experiments relative to corresponding BDI sensors. The results demonstrate that the measurement derived from both systems are comparable, but the DIC results exhibit a noisier response. This outcome is expected, but it should also be noted that the full-field measurement capability derived from DIC cannot be achieved with local sensing techniques and the full-field measurement provides a unique capability for a more robust St-ID strategy. During the experiments, the DIC measurement also provided a supplemental benefit to the investigation in that vertical deflections were measured at the support locations, which were previously assumed to be fixed in this direction.

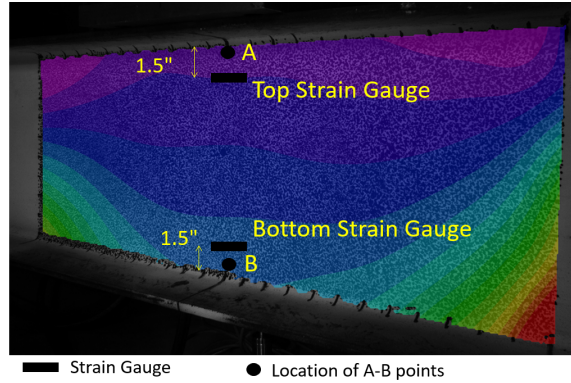


Figure 10 - Longitudinal (ϵ_{xx}) DIC strain fields at the maximum load, $t=150$ sec, frame#300

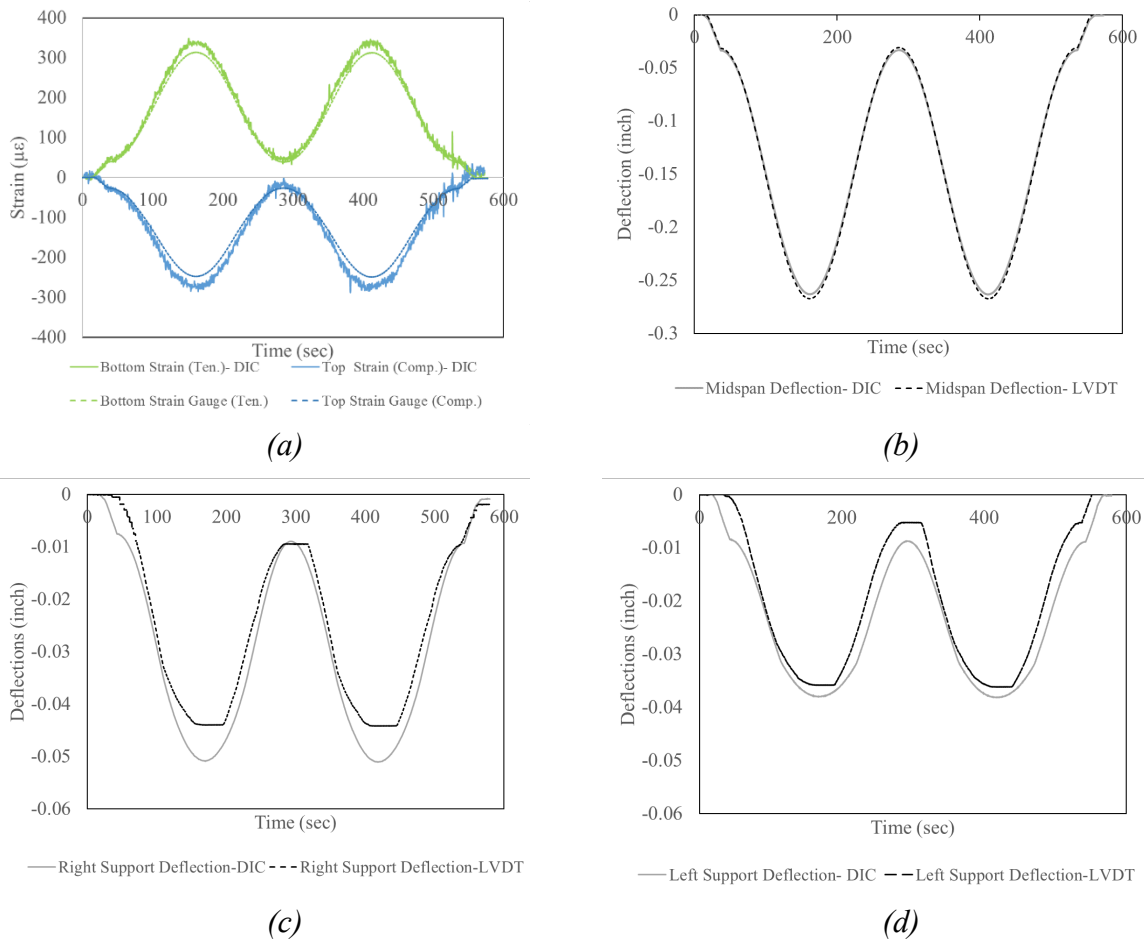


Figure 11 - Comparison of results obtained from DIC and mechanical sensors (a) midspan strain; (b) midspan deflection; (c) right support deflection; (d) left support deflection

Structural identification using FEMU with DIC via hybrid optimization algorithm

In the initial phase of this study [39], limited non-full-field data derived from DIC measurements were used in an FEMU scheme, but the sparse data used in the refinement was not sufficient for consistent model updating. However, DIC provides a rich data set for evaluation when compared to physical sensors and the full-field measurement derived from DIC provided a rational mechanism for performing multi-objective optimization for model updating.

The initial FE models, developed in parallel with the experimental configurations, were updated using an optimization algorithm (Hybrid Genetic Algorithm (HGA)) to converge on predictions of the beam's Young's Modulus (E_s) and support stiffness parameters (K_1, K_2, K_3, K_4). As illustrated in Figure 4, three scenarios were selected for model updating with variations in the restraint conditions and objective function parameters. The optimization algorithm developed in this investigation incorporated the features of a genetic algorithm and a gradient-based scheme to iterate on the unknown parameters.

Definition of the objective function

The identification problem consists of the determination of structural parameters that minimize the difference between calculated data from a numerical model and a set of experimental data. In this research, the numerical model was a finite element model with the same geometry and boundary conditions as the experimental setup. The identification leveraged a generalized cost function (Equation 2) to evaluate agreement between the numerical and experimental results.

$$F = \frac{1}{N_i} |y_i^{num} - y_i^{exp}| \quad \text{Equation 2}$$

Where F is the cost function, y_i^{num} is the i -th information obtained with the numerical simulation, y_i^{exp} is the i -th information obtained with the set of experiments conducted and N_i is a weight factor. In this study, the experimental data utilized for the definition of the cost function were the strain and displacement fields; however, other measurement data could also have been included in the St-ID process.

For comparison of the results from these two analyses, a common grid was required to ensure that the measurement/analysis locations were spatially equivalent. To achieve a common reference for comparison between the FEA and DIC results, it was necessary to interpolate the results from DIC grid over the FEA grid (or vice versa). The interpolation was performed using MATLAB and a general mesh grid was defined, with the spatially positioned results from FEM and DIC are interpolated onto the newly defined mesh. A bilinear interpolation algorithm was developed for this process, where interpolated values of the new grid were obtained based on the values of the four nearest neighbors forming a quad surrounding the interpolated point. Following the alignment of the experimental and numerical results onto a common grid, a final version of the cost function was formulated (Equation 3).

$$F = \sum_i \sum_t \left(\frac{|\varepsilon_{xx}^{num} - \varepsilon_{xx}^{exp}|}{\varepsilon_{xx}^{exp}} \right)^2 + \sum_i \sum_t \left(\frac{|\varepsilon_{xy}^{num} - \varepsilon_{xy}^{exp}|}{\varepsilon_{xy}^{exp}} \right)^2 + \sum_i \sum_t \left(\frac{|\delta_{xx}^{num} - \delta_{xx}^{exp}|}{\delta_{xx}^{exp}} \right)^2 \quad \text{Equation 3}$$

where $\varepsilon_{xx}^{exp}, \varepsilon_{xy}^{exp}$ and δ_y^{exp} represent the two components of the strain tensor and displacement, respectively that are extracted at a point i of coordinates x_i at time t . The values $\varepsilon_{xx}^{num}, \varepsilon_{xy}^{num}$ and δ_y^{num} represent the corresponding values computed from the finite element model. Data for three representative time frames, namely $t=100, 150, 175$ sec., were selected for evaluation using the proposed cost function and provided a basis for representation of different

stages of loading while maintaining a reasonable computational cost. It should be noted that additional loading steps (time steps) could be included to increase the robustness; however, these additional steps were not deemed necessary with the beam remaining in the elastic range during testing.

Optimization Process- Hybrid Genetic Algorithm (HGA)

The hybridized training algorithm adopted to minimize the cost function (Equation 3) and derive unknown parameters (E_s, K_1, K_2, K_3, K_4) was based on the combination of a Genetic Algorithm (GA) and a gradient-based algorithm. Both the GA and gradient-based techniques are well-established optimization methods and have been used in numerous optimization problems [40]; however, previous literature has shown that for problems involving a large number of parameters, a combination of these two techniques yields superior optimization performance [41]. Figure 12 illustrates a basic flowchart of the HGA procedure adopted in this work.

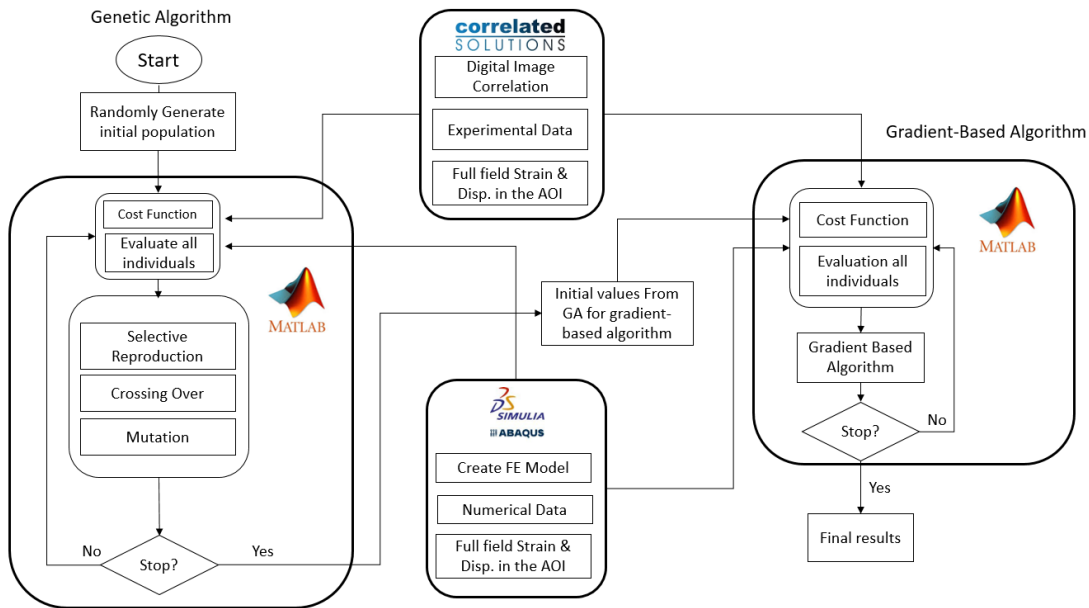


Figure 12 - Overview of the proposed Hybrid-Genetic Algorithm

Table 1 shows the initial values selected within the feasible range (maximum and minimum values) used as the initial guess for the parameters in the HGA procedure. Table 2 presents three representative sets of training parameters used within the GA based on literature [42, 43]. For the parameters used in the algorithm, N_{pop} represents initial population, N_{elites} represents population of elites which relate directly to the next generation, N_{mut} represents the population which are randomly selected for mutation, μ represents the probability rate of mutation, N_{pairs} represents as selecting parents for mating, and $iterations$ describe a stopping criteria for termination. The optimization process represents a trade-off between computational time and solution accuracy and the parameters selected in this study only represent three optimization scenarios selected for evaluation of the validity of the approach rather than convergence to the exact solution. A more extensive study on optimization was deemed beyond the scope of this work.

Table 1 - Initial, minimum and maximum values of the updating parameters

Material parameter	E_s (ksi)	K_1 (lb/in.)	K_2 (lb/in.)	K_3 (lb in./rad)	K_4 (lb in./rad)
Initial	25,000	70,000	70,000	2,000	2,000
min	20,000	50,000	50,000	50	50
max	40,000	150,0000	150,0000	5,000	5,000

Table 2 - Parameters of the genetic algorithm (GA) for the three identification tests for the first configuration

GA Parameter Group (PG)	N_{pop}	N_{elites}	N_{mut}	μ	N_{pairs}	Iterations
A	10	1	2	0.04	7	40
B	20	2	4	0.04	14	20
C	50	4	8	0.04	28	20

Solution Convergence

Configuration 1 (CF1) was used to evaluate the performance and efficiency of the parameter groups presented in Table 2. Herein, performance represents the capability to converge to a rational solution of E_s (assumed to be 29,000 ksi) at the global minima, with efficiency described by the time of solution. An illustration of the solution efficiency is shown in Figure 13, which highlights the evolution of the cost function as the parameters converge towards their optimal solution. As shown, the GA training was terminated in each case at 20 epochs where an obvious plateau in the cost function and parameters was observed. At this point, the gradient-based algorithm was initiated, which further minimized the cost function and resulted in convergence to the final solution. Table 3 includes the parameter results of the optimization solutions for this configuration. The results demonstrate that *CFIB* and *CFIC* both exhibit satisfactory performance when compared to *CFIA*, but the computational cost (solution time) for *CFIC* is much higher without a significant improvement in performance. It should be highlighted that *CFIA* does not approach a rational solution for E_s and appears to be stuck at some local minima, highlighting the importance of the number of individuals (N_{pop}) used in the first generation of the hybrid-optimization algorithm.

Table 3 - Identified optimal parameters based on Hybrid Genetic Algorithm for different parameters of the GA for the first configuration

Configuration/ PG	E_s (ksi)	K_1 (lb/in.)	K_2 (lb/in.)	K_3 (lb in./rad)	K_4 (lb in./rad)	Solution time (Hour)
<i>CFIA</i>	27,488	92,551	90,165	125	188	20
<i>CFIB</i>	29,100	97,416	90,020	80	54	20
<i>CFIC</i>	29,244	98,018	88,000	55	66	50

As noted convergence for each of the final parameter selections manifested as a plateau in each parameter. For the modulus of elasticity parameter, the rational solution for steel provided a reference for comparison; however, for the restraint conditions no such comparison was available. To evaluate the final parameters for the boundary restraints, a limited convergence study was

performed to correlate the degree of model restraint relative to the idealized solution. For the pin-roller condition, the expectation was zero rotational restraint and infinite vertical restraint, whereas the expectation for the fixed condition maintained that same vertical restraint, but included infinite rotational restraint.

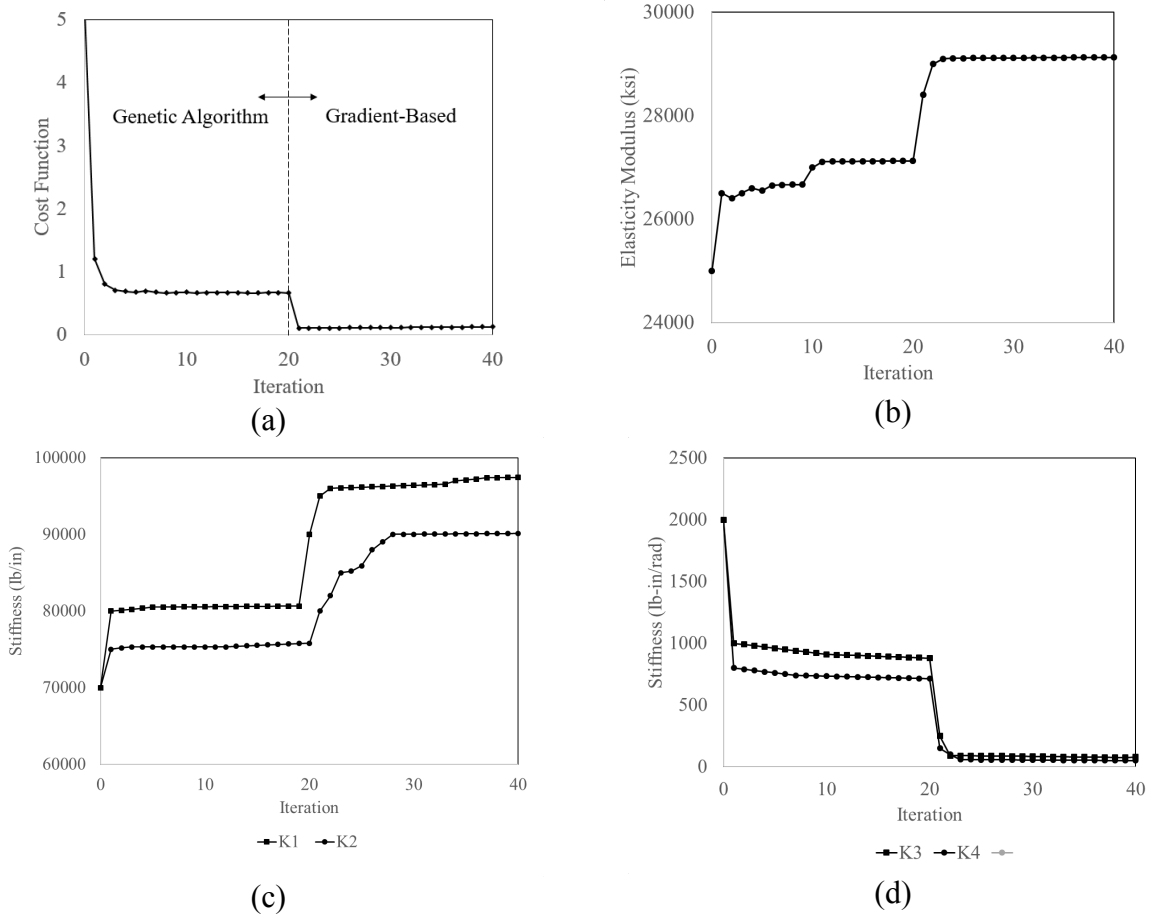


Figure 13 - Evolution of unknown parameter convergence versus iterations for CF1B (a) Cost Function (b) Modulus of Elasticity (c) K_1, K_2 (d) K_3, K_4

The boundary condition convergence study used the finite element model of the test beam with the boundary restraint stiffness values parameterized. Using the model, the values of the boundary restraints (e.g. K_1 / K_2 and K_3 / K_4) were varied iteratively to establish the upper and lower bounds of the restraint stiffness required to mimic the idealized solutions (i.e. simple and fixed conditions). This idealized solution was realized when the selected degree of freedom converged to a plateau, indicating additional restraint stiffness does not yield additional restraint resistance. The resulting convergence study demonstrated that a fixed vertical restraint stiffness equated to 5,000 lb/in, whereas full rotational restraint equated to 250,000 lb in./rad. With the rationality of the optimized parameters established, it was determined that the parameter group B yielded the most efficient optimization solution and was selected for evaluation of the other two configurations (CF2 and CF3). Using this parameter group, the final identified parameters are presented in Table 4 for all three test configurations.

Table 4 - Identified optimal parameters for different configurations for group B set of parameters of the GA

Configuration/ PG	E_s (ksi)	K_1 (lb/in.)	K_2 (lb/in.)	K_3 (lb in./rad)	K_4 (lb in./rad)
CF1B	29,100	97,416	90,020	80	54
CF2B	29,411	98,001	92,445	81	74
CF3B	30,049	148,7774	147,8891	241	1,800

A comparison between the full-field contours of the DIC and the updated FE model are presented in Figure 14 and Figure 15 for the midspan and support locations, respectively for CF1B. Figure 14 illustrates a comparison of the longitudinal strain (ϵ_{xx}), shear strain (ϵ_{xy}), and vertical deflection (δ_y). From this comparison, it is evident that the updated model is able to reproduce the responses derived from the experiment as illustrated by the minimal error exhibited within the area of interest. It should be noted that the localized errors in the longitudinal strain contours are associated with local stress concentrations that occur on the top of the beam at the location of the load application. Figure 15 illustrates a comparison of the deflections for the two end locations. It is also notable that while the vertical deflection right above the supports were initially expected to be zero, some support settlement can be seen in the results. Similar to the midspan location, the error between the DIC measurement and updated model is minimal across the area of interest. Similar results were derived for CF2B and CF3B, but are not included in this report for brevity.

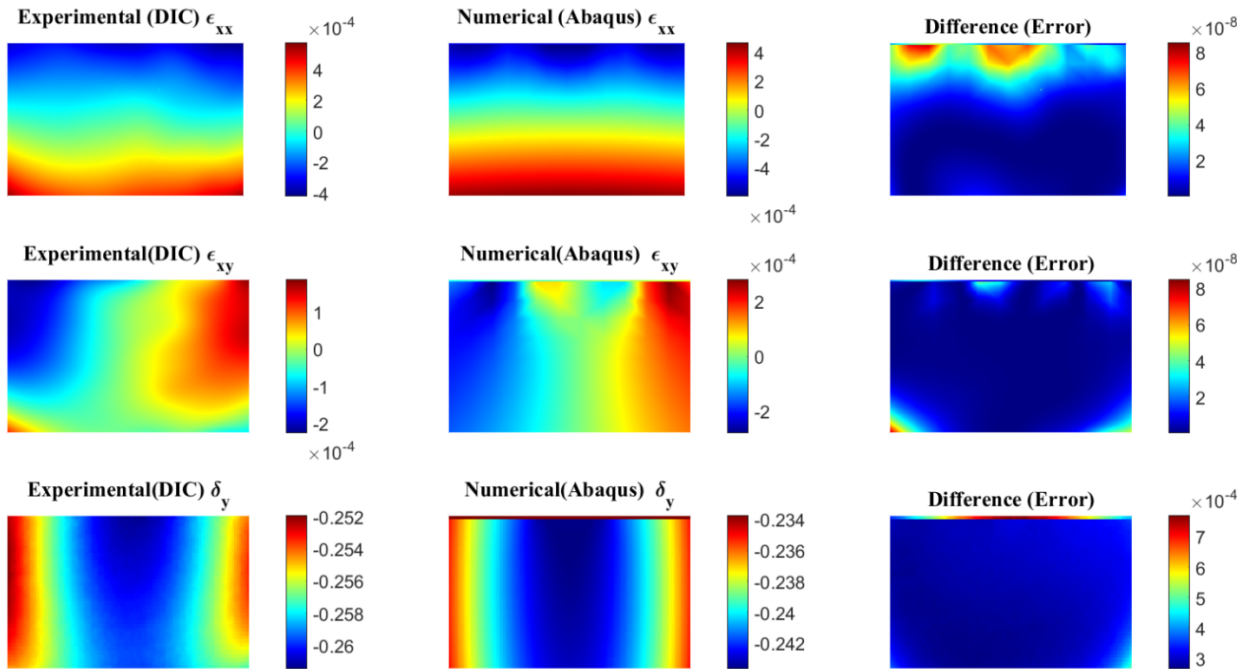


Figure 14 - Contour plots of the experimental strain fields, the numerical strain fields and their absolute difference for the middle span for the components ϵ_{xx} , ϵ_{xy} , δ_y at $t=150$ sec for CF1B

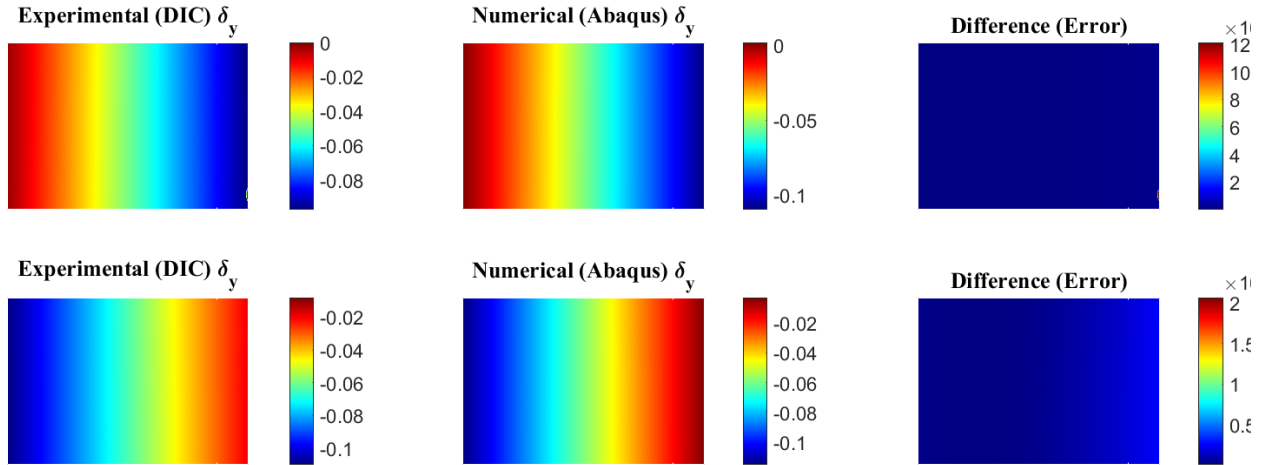


Figure 15 - Contour plots of the experimental strain fields, the numerical strain fields and their absolute difference for the component δ_y (first row for left support and second row for right support) at $t=150$ sec for CF1B

Performance of Updated FE Model

To evaluate the efficiency of the identification procedure, the performance of the model before and after updating were compared to the results derived from the experiments. For this evaluation, two points of interest for CF1B were selected for comparison, namely points A and B which were previously illustrated in Figure 10. The temporal evolution of the longitudinal strain both before and after the updating process are shown in Figure 16a and Figure 16b, respectively. Comparing the results from the updated model with those derived from the DIC measurements demonstrate the success of the identification procedure, in that the revised strain response now tracks along with those derived from the experiment. It can be seen that the evolution of local strain is correctly described over the entire loading sequence, with comparable magnitudes and falls within about 8% error window of the measured response. Similar results were derived for CF2B and CF3B, but are not included in this report for brevity.

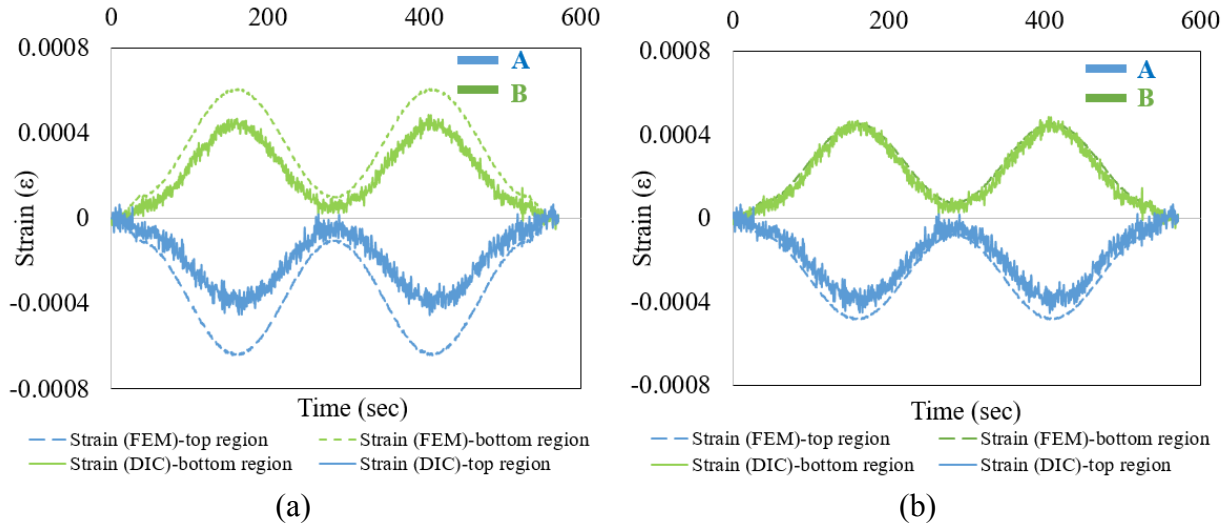


Figure 16 - Comparison of the evolution of the longitudinal strains ϵ_{xx} for CFB1 between the numerically computed values and the values obtained using DIC at points A-B shown in fig. 8, for (a) before model updating, (b) after updating

CONCLUSION

This report presents the results of a study on structural identification to identify the material properties and boundary conditions using full field measurements derived from 3D digital image correlation (3D-DIC). The outcomes demonstrate that full-field measurement techniques are sufficiently robust for use within a St-ID framework for SHM. This report describes the core components of the proposed full-field St-ID process including the experimental setup, numerical model development, creation of common reference plan, and model updating. Based on the findings of this primarily laboratory study, the following conclusions can be drawn:

- The St-ID results obtained in this work suggest that image-based measurements sensing using 3D-DIC can be successfully used as an alternative to physical in-place sensors for characterizing the response of large scale structural systems. Overall, the excellent agreement of the strain and displacement responses achieved after the completion of the updating process confirmed the efficacy of the proposed identification method. The observed advantage in the developed full-field approach is expected to enable to use of a reduced sensor suite for St-ID as the rich data derive across the surface is more informative than a local sensing approach.
- Features observed using 3D-DIC are available in post-processing, allowing for the identification of unforeseen behavior. In this work, support deflections were identified from the 3D-DIC measurements and would have gone unmeasured using a traditional sensing if this response was not expected a priori.
- The spatial correspondence between the DIC measurements and finite element simulation results provides a basis for further identification of highly localized features that may not present in local sensor measurements. An example of this phenomena was present when evaluating the local strain concentrations that manifested at the location of the load application.

RECOMMENDATIONS AND FUTURE WORK

Based on the outcomes of this study, it is evident that there is great potential for leveraging 3D-DIC as a tool for efficient St-ID. The study evaluated the feasibility of this technique using a limited experimental program. Future work in this area should evaluate the robustness of the proposed framework on more complex structural systems. This complexity should include large scale structural systems with more complex load sharing characteristic, variations in materials used and additional uncertainty in the condition state and boundary conditions. During this study, the project team also explored the potential for enhancing the robustness of identification of unknown parameters by incorporating measurable damage features into the framework. This extension provides a pathway for future work in the area of identification of unseen damage using the same basic St-ID approach.

REFERENCES

- [1] Federal Highway Administration (FHWA). National Bridge Inventory (NBI) Database. Washington, D.C.: Federal Highway Administration; 2017.
- [2] Sohn H, Farrar CR, Hemez FM, Shunk DD, Stinemates DW, Nadler BR et al. A review of structural health monitoring literature: 1996-2001. Los Alamos, NM: Los Alamos National Laboratory; 2004.
- [3] Aktan AE, Catbas FN, Grimmelsman KA, Tsikos CJ. Issues in infrastructure health monitoring for management. *Journal of Engineering Mechanics*. 2000;126:711-24.
- [4] Ahlborn T, Shuchman R, Sutter L, Brooks C, Harris D, Burns J et al. *The State-of-the-Practice of Modern Structural Health Monitoring for Bridges: A Comprehensive Review*. 2010.
- [5] Vaghefi K, Oats R, Harris D, Ahlborn T, Brooks C, Endsley K et al. Evaluation of Commercially Available Remote Sensors for Highway Bridge Condition Assessment. *Journal of Bridge Engineering*. 2012;17:886-95.
- [6] Webb G, Vardanega P, Middleton C. Categories of SHM Deployments: Technologies and Capabilities. *Journal of Bridge Engineering*. 2014;10.1061/(ASCE)BE.1943-5592.0000735:04014118.
- [7] Gangone MV, Whelan MJ, Janoyan KD, Jha R. Field deployment of a dense wireless sensor network for condition assessment of a bridge superstructure. *SPIE 6933: Smart Sensor Phenomena, Technology, Networks, and Systems*. Bellingham WA: International Society for Optical Engineering - SPIE; 2008. p. 69330.
- [8] Loh KJ, Lynch JP, Kotov NA. Mechanical-electrical characterization of carbon-nanotube thin films for structural monitoring applications. *Proceedings of the SPIE - The International Society for Optical Engineering*. 2006:61741Z-1-12.
- [9] Shamim NP, Gregory LF, Sukun K, David EC. Design and Implementation of Scalable Wireless Sensor Network for Structural Monitoring. *Journal of Infrastructure Systems*. 2008;14:89-101.
- [10] Bartoli G, Facchini L, Pieraccini M, Fratini M, Atzeni C. Experimental utilization of interferometric radar techniques for structural monitoring. *Structural Control and Health Monitoring*. 2008;15:283-98.

- [11] Doebling SW, Farrar CR, Prime MB. Summary review of vibration-based damage identification methods. *Shock and Vibration Digest*. 1998;30:91-105.
- [12] Vaghefi K, Oats R, Harris D, Ahlborn T, Brooks C, Endsley K et al. Evaluation of Commercially Available Remote Sensors for Highway Bridge Condition Assessment. *Journal of Bridge Engineering*. 2011;17:886-95.
- [13] Ribeiro D, Calçada R, Delgado R, Brehm M, Zabel V. Finite element model updating of a bowstring-arch railway bridge based on experimental modal parameters. *Engineering Structures*. 2012;40:413-35.
- [14] Friswell M, Mottershead JE. *Finite element model updating in structural dynamics*: Springer Science & Business Media; 2013.
- [15] Zapico J, Gonzalez M, Friswell M, Taylor C, Crewe A. Finite element model updating of a small scale bridge. *Journal of Sound and Vibration*. 2003;268:993-1012.
- [16] Sanayei M, Phelps JE, Sipple JD, Bell ES, Brenner BR. Instrumentation, nondestructive testing, and finite-element model updating for bridge evaluation using strain measurements. *Journal of bridge engineering*. 2011;17:130-8.
- [17] Schlune H, Plos M, Gylltoft K. Improved bridge evaluation through finite element model updating using static and dynamic measurements. *Engineering structures*. 2009;31:1477-85.
- [18] Bischoff PH, Perry SH. Compressive behaviour of concrete at high strain rates. *Materials and Structures*. 1991;24:425-50.
- [19] Cuccovillo T, Coop M. The measurement of local axial strains in triaxial tests using LVDTs. *Géotechnique*. 1997;47.
- [20] Neild S, Williams M, McFadden P. Development of a vibrating wire strain gauge for measuring small strains in concrete beams. *Strain*. 2005;41:3-9.
- [21] Whiteman T, Lichti D, Chandler I. Measurement of deflections in concrete beams by close-range digital photogrammetry. *Proceedings of the Symposium on Geospatial Theory, Processing and Applications: ISPRS Commission IV Ottawa, ON, Canada; 2002*. p. 9-12.
- [22] Maas H-G, Hampel U. Photogrammetric techniques in civil engineering material testing and structure monitoring. *Photogrammetric Engineering & Remote Sensing*. 2006;72:39-45.
- [23] Hampel U, Maas H-G. Application of digital photogrammetry for measuring deformation and cracks during load tests in civil engineering material testing. *Optical 3-D Measurement Techniques VI*. 2003;2:80-8.
- [24] Peters W, Ranson W. Digital imaging techniques in experimental stress analysis. *Optical engineering*. 1982;21:213427--.
- [25] Peddle J, Goudreau A, Carson E, Santini-Bell E. Bridge displacement measurement through digital image correlation. *Bridge Structures-Assessment, Design & Construction*. 2011;7.
- [26] Yoneyama S, Kitagawa A, Iwata S, Tani K, Kikuta H. Bridge deflection measurement using digital image correlation. *Experimental Techniques*. 2007;31:34-40.
- [27] Citto C, Wo SI, Willam KJ, Schuller MP. In-Place Evaluation of Masonry Shear Behavior Using Digital Image Analysis. *ACI Materials Journal*. 2011;108.
- [28] Lawler JS, Keane DT, Shah SP. Measuring three-dimensional damage in concrete under compression. *ACI Materials journal*. 2001;98.
- [29] Xiao J, Li W, Sun Z, Shah SP. Crack propagation in recycled aggregate concrete under uniaxial compressive loading. *ACI Materials Journal*. 2012;109.
- [30] Ghrib F, El Ragaby A, Boufama B, Li L, Memar S. A Novel Technique for Displacement Measurements in RC Beams using Digital Image Correlation. *ACI Special Publication*. 2014;298.

- [31] Murray C, Hoag A, Hoult NA, Take WA. Field monitoring of a bridge using digital image correlation. *Proceedings of the ICE - Bridge Engineering*2015. p. 3-12.
- [32] Vaghefi K, Ahlborn T, Harris D, Brooks C. Combined Imaging Technologies for Concrete Bridge Deck Condition Assessment. *Journal of Performance of Constructed Facilities*. 2015;29:04014102.
- [33] Lattanzi D, Miller GR. Robust automated concrete damage detection algorithms for field applications. *Journal of Computing in Civil Engineering*. 2012;28:253-62.
- [34] Sutton MA, Orteu JJ, Schreier H. *Image correlation for shape, motion and deformation measurements: basic concepts, theory and applications*: Springer Science & Business Media; 2009.
- [35] Alipour M, Washlesky SJ, Harris DK. Field Deployment and Laboratory Evaluation of 2D Digital Image Correlation for Deflection Sensing in Complex Environments. *Journal of Bridge Engineering*. 2019;24:04019010.
- [36] Dizaji MS, Harris DK, Alipour M, Ozbulut OE. Reframing measurement for structural health monitoring: a full-field strategy for structural identification. *Nondestructive Characterization and Monitoring of Advanced Materials, Aerospace, Civil Infrastructure, and Transportation XII: International Society for Optics and Photonics*; 2018. p. 1059910.
- [37] Dizaji MS, Alipour M, Harris D. Leveraging Full-Field Measurement from 3D Digital Image Correlation for Structural Identification. *Experimental Mechanics*. 2018:1-18.
- [38] Shafiei Dizaji M, Harris D, Alipour M, Ozbulut O. En “vision” ing a novel approach for structural health monitoring—a model for full-field structural identification using 3D–digital image correlation. *The 8th International Conference on Structural Health Monitoring of Intelligent Infrastructure, Bridbane, Australia*2017. p. 5-8.
- [39] Dizaji MS, Alipour M, Harris DK. *Leveraging Vision for Structural Identification: A Digital Image Correlation Based Approach*. International Digital Imaging Correlation Society: Springer; 2017. p. 121-4.
- [40] Goldberg D. *Genetic Algorithms in Search, Optimization and Machine Learning*, Addison-Wessley Professional. Reading, USA. 1989.
- [41] Jung D-S, Kim C-Y. Finite element model updating of a simply supported skewed PSC I-girder bridge using hybrid genetic algorithm. *KSCE Journal of Civil Engineering*. 2013;17:518-29.
- [42] Joghataie A, Farrokh M. Dynamic analysis of nonlinear frames by Prandtl neural networks. *Journal of engineering mechanics*. 2008;134:961-9.
- [43] Farrokh M, Dizaji MS, Joghataie A. Modeling hysteretic deteriorating behavior using generalized Prandtl neural network. *Journal of Engineering Mechanics*. 2015;141:04015024.